Catena 142 (2016) 245–251

Contents lists available at ScienceDirect

Catena

journal homepage: www.elsevier.com/locate/catena

Smartstones: A small 9-axis sensor implanted in stones to track their movements

Oliver Gronz [a,*], Priska H. Hiller [b], Stefan Wirtz [a], Kerstin Becker [a], Thomas Iserloh [a], Manuel Seeger [a], Christine Brings [a], Jochen Aberle [b], Markus C. Casper [a], Johannes B. Ries [a]

[a] Department of Physical Geography, Trier University, 54286 Trier, Germany
[b] Department of Hydraulic and Environmental Engineering, Norwegian University of Science and Technology NTNU, S. P. Andersens veg 5, 7491 Trondheim, Norway

ARTICLE INFO

Article history:
Received 29 April 2015
Received in revised form 8 January 2016
Accepted 24 March 2016
Available online 6 April 2016

Keywords:
Active tracer
Geomorphology
Hydraulic engineering
Stone movement
Active RFID (radio frequency identification)

ABSTRACT

The movement of stones is important in a variety of disciplines such as geomorphology or hydraulic engineering. Plenty of different sensors, visual, active or passive tracers exist to capture movements in various ways. However, none of them is sufficiently small to be implanted in pebbles with a longest axis of approx. 60 mm.

In this article, a sufficiently small probe is introduced: the Smartstone probe. It consists of a metal cylinder (diameter 8 mm, length 55 mm) with a flexible antenna and contains a Bosch BMX055 sensor composed of a triaxial accelerometer, magnetometer and gyroscope, respectively. Additional components inside the probe are memory to store data, active RFID (Radio-frequency identification) technique to transmit data and two button cells as power supply.

Mounted into a pebble, the applicability of this probe was tested in laboratory flume experiments by determining the pebble movement using the Smartstone measurements and comparing them to the movement pattern captured by a high-speed camera. The derived orientations and positions in these test experiments resulted in deviations of 32.4% compared to the visual footage. The different reasons for deviations are noise, quantization error, integration error, orientation error and clipping. The error sources were divided with supplementary experiments resulting in mean absolute deviation (MAE) of 3.3% due to noise, quantization, and integration errors; orientation errors result in an increased MAE of 13.7% in natural environment and 21.7% in laboratory. The MAE of all experiments containing clipping was 63.2%.

These deviations will be reduced in future by application of methods like Kalman filtering or Markov models, which are established in other disciplines like computer science, robotics or (pedestrian) navigation.

1. Introduction

Movements of stones are an important part of several geomorphological and hydrological processes as well as engineering applications. This includes fast movements like rockfalls or other mass movements in high mountain regions, slower movements in fluvial and glacial environments, and erosion protection measures.

To identify stone movements, different methods have been developed and applied in earlier research. This includes visual tracers such as coloured rocks (De Jong, 1991; Foster, 2000) or fluorescent dye (Cameron, 2012), passive or active tracers (Cameron, 2012; Ergenzinger and De Jong, 2003; Gray et al., 2010; Ryan et al., 2005), sediment traps (Ergenzinger et al., 1994; Habersack, 1997; Reid et al., 1980; Schaffernak, 1916), video observation (Krause, 1997), acoustic sensors (Bedeus and Ivicsics, 1963; Johnson and Muir, 1969; Krein et al., 2008), as well as recent applications like Passive Integrated Transponder (PIT) tags (Ergenzinger et al., 1989; Lamarre and Roy, 2008; Liébault et al., 2012; Oikawa, 2011; Schneider et al., 2010).

All these methods have limitations impeding a thorough observation of the transportation path, movement types and forces affecting the ground. Recently developed PIT tags have made significant progress towards a thorough observation, but have mainly been developed for the monitoring of bigger stones and boulders. For the observation of smaller stones, a system is still missing. Moreover, the measurement of the acceleration that a stone experiences at incipient motion conditions would allow for calculating the resulting force acting on the stone. This would deepen our understanding of the erosion process itself. A more specific application is the design of slope protections with riprap,

* Corresponding author.
E-mail addresses: gronz@uni-trier.de (O. Gronz), priska.hiller@ntnu.no (P.H. Hiller), wirtz@uni-trier.de (S. Wirtz), k.becker0712@gmx.de (K. Becker), iserloh@uni-trier.de (T. Iserloh), seeger@uni-trier.de (M. Seeger), brings@uni-trier.de (C. Brings), jochen.aberle@ntnu.no (J. Aberle), casper@uni-trier.de (M.C. Casper), riesj@uni-trier.de (J.B. Ries).

http://dx.doi.org/10.1016/j.catena.2016.03.030

where such information may be helpful for the development of improved design approaches.

To avoid the limitations, a sensor carrier was developed for stones including an active radio-frequency identification (RFID) chip, an accelerometer, a magnetometer and a gyroscope. Developer was the company SST (smart sensor technologies) in Rheinberg, Germany for the Department of Physical Geography at Trier University in cooperation with the Department of Hydraulic and Environmental Engineering at the Norwegian University of Science and Technology, NTNU Trondheim. The probe uses a protocol protected by patent US20140240088. However, the data analysis described in the sample application of this technical note is open for further developments.

The relatively compact dimensions of the Smartstone probe (described in Section 2) allow its insertion into larger pebbles. This subsequently called "Smartstone" can be used as an advanced RFID-based tracer stone. Such tracer stones have a wide application range from laboratory use to fluvial environments. For example, within the laboratory, such tracer stones may be used to acquire directly data on the movement of individual particles with a high temporal resolution, i.e. to study sediment transport mechanics without the need of visual access to the particles (e.g. photogrammetry). Within field applications, much more detailed information can be extracted from RFID-based tracer stones than by "conventional" tracer stones given the stones can be adequately contacted via gateways along the transport path and that the battery lifetime is adequate. Last but not least, the RFID technology is helpful for the localisation of tracer stones as the probe can still receive radio signals even if it is in sleeping mode.

The main objectives of this article are to:

- describe the Smartstone probe, its specification and usage,
- describe an exemplary laboratory flume experiment demonstrating the probe's capabilities and present limitations,
- discuss the measuring principle by means of an application.

2. Description of the Smartstone system

2.1. Probe specifications

The Smartstone prototype kit consists of the Smartstone probe, a gateway, an optional wireless router, and a computer for data communication. The Smartstone probe is a 55 mm long and 8 mm wide cylinder with a 70 mm long flexible antenna (Fig. 1a). It weighs 0.0075 kg including battery. The self-calibrating probe is powered by two silver-oxide button cells (1.55 V, 20 mAh) and contains the core unit of the Smartstone-kit: a BMX055 sensor module. This module comprises a triaxial 12 bit acceleration sensor, a triaxial 16 bit gyroscope, and a geomagnetic sensor (sometimes also referred to as e-compass or geomagnetic sensor), together with an active RFID tag, 261.92 kB memory, a chronometer, and a thermometer. The sensor module data provides orientation, tilt, motion, acceleration, rotation, shock, vibration and heading of the probe (Bosch Sensortec, 2014). The chronometer and thermometer provide auxiliary data on time (resolution 1/32,768 s) and temperature. For the presented prototype, the ranges of the sensor module are +/−4 g for the accelerometer (where g denotes the acceleration due to gravity), +/−2500 μT for the magnetometer (where T denotes the unit Tesla), and +/−2000° s^{-1} for the gyroscope. One sensor axis is aligned with the long axis of the cylinder, the other two axes orientations are indicated by the battery screw (Fig. 1b).

2.2. Data transmission

The sensed data are transferred to a Linux-based gateway via an 868 MHz radio antenna. The gateway uses a SSH (Secure Shell) server to enable controlling the probes. Additionally, it stores the data (of several probes) in a database. The sensed data are either forwarded to a wireless router at a frequency of 2.4 GHz or directly to a computer connected with an Ethernet cable. The data transfer from the gateway is based on the Hypertext Transfer Protocol (HTTP), so that the data can be directly assessed and post-processed using mathematical software or spreadsheet applications. If several Smartstone probes are used simultaneously, the data are assigned to the specific probes via the RFID tag. The data transfer is managed via a specific software developed by SST.

The radio frequency (RF) transmitted data from the probe to the gateway includes information on date and time, temperature, battery voltage, memory fill level, probe ID (RFID-tag), and measurement mode.

2.3. Probe setup options

The probe has different modes indicating recording, standby, and configuration. In recording mode, impacts are recorded with very short response times. After a period with impacts below a user-defined threshold, the probe switches to standby mode with reduced power consumption. From standby mode, the probe switches either to recording mode through new impacts or to configuration mode after longer periods without further impacts. The time intervals for automatically switching between the modes and the impact thresholds are software-defined and can be adapted with regard to individual applications.

The configuration mode can be used for active communication with the probe to synchronize the time with the gateway, to activate/deactivate individual sensors (i.e. accelerometer, magnetometer or gyroscope), to read out or clear the memory, and to define the selection of the aforementioned thresholds. Moreover, the configuration mode allows also selecting between different settings varying in power consumption and accuracy. In total, four different power settings can be chosen. The setting with lowest power consumption results in a noise of 10 mg for the accelerometer, 2 μT for the magnetometer, 2° s^{-1} for the gyroscope. On the other side of the spectrum, the setting with lowest noise and highest power consumption results in a noise of 1.2 mg for the accelerometer, 0.5 μT for the magnetometer and 0.24° s^{-1} for the gyroscope. More detailed information is given in the data sheet (Bosch Sensortec, 2014). The description also contains information about the

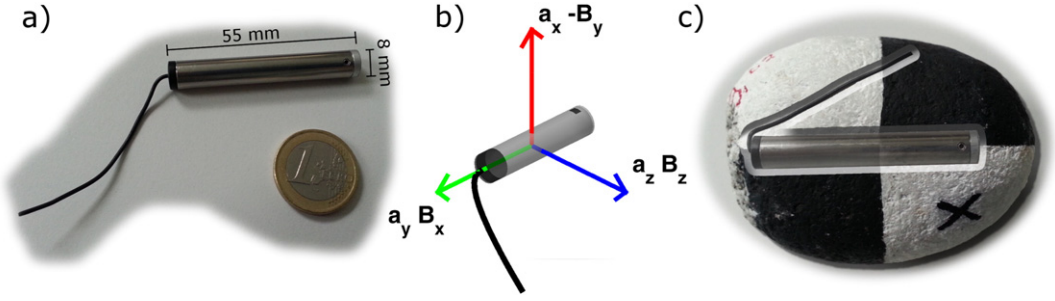

Fig. 1. a) The Smartstone probe and its dimensions, b) three dimensional coordinate systems of the acceleration sensor (a_x, a_y, a_z) and the geomagnetic sensor (B_x, B_y, B_z), black point indicates battery screw, c) artist-illustration of the probe inserted into a tracer pebble.

applied filters and the discretization resulting from different accelerometer ranges.

The prototype probe presented in this paper allows for sampling intervals ranging from 12 ms to 100 ms. Using sampling intervals shorter than 100 ms precludes acquisition of gyroscope data due to the relatively large response time of the gyroscope. Therefore, operation of the gyroscope depends on the expected stone (rotation) velocity: If rotation velocity exceeds five rotations per second, sub-Nyquist sampling does not allow for derivation of velocities.

3. Preliminary tests

3.1. Data transmission range

The distance in which a Smartstone probe remains in regular contact with the gateway is considered as functional range. If this distance is exceeded, the probe has irregular contact with the gateway until the signal transfer finally stops, i.e. the maximum range is reached. The functional and maximum signal ranges of the Smartstone probe through air were evaluated by moving the probe stepwise away from the gateway. The functional range with intervisibility was 220 m (max. range 280 m). However, any disturbance, like plants, buildings, walls, will decrease those ranges.

To examine the effect of bodies in which the probe is embedded, the range experiments were repeated with the probe being inserted into stones of different sizes and materials:

1. Pebble (which is later used in the experiments in Section 3.3): longest axis 76 mm, short axis 46 mm, and 57 mm along the middle axis; density 2680 kg m^{-3}; granite; two holes like described in Section 3.3.2; functional range with pebble-gateway intervisibility 48 m.
2. Cobble: 155 mm × 90 mm × 110 mm; density 2640 kg m^{-3}; granite; one borehole with depth 105 mm (centred sensor) with the antenna routed like a spiral spring in the same hole, rest of hole filled with drilling dust resulting from the specific stone and modelling mass cap; functional range with intervisibility 52 m.
3. Cubic paving stone: all axes approx. 90 mm; density 2810 kg m^{-3}; basalt (iron-rich); one borehole (depth 72.5 mm) with antenna routed like a spiral spring in the same hole, drilling dust, modelling mass; functional range with intervisibility 50 m.

The results of these tests show that the routing of the antenna has a stronger influence than the body-diameter and that the antenna elongating the probe cylinder is better than a side-by-side position.

The data transmission under water was tested in a small natural lake with the gateway being placed at the lakefront and using the aforementioned pebble. In this test, the transmission was still working at the lake's maximum depth of 1.15 m. Additional tests at different environments showed a stronger influence of surrounding: in a sufficiently deep lock chamber with armoured concrete walls, data transmission stopped working at 0.4 to 0.5 m. In an underground water storage in a building (armoured concrete walls, metal doors), the signal transmission did not work at all.

These tests thus showed that the influence of the environment is stronger than the water depth and that especially metal and armoured concrete decrease the range. Therefore, before using the probe in a specific environment, preliminary range tests should be carried out.

It is worth mentioning that exceeding the maximum transmission range does not result in data loss: the probe works autonomously without gateway. Communication with the gateway is only necessary to adjust settings or to transfer data stored in the probe's own memory.

3.2. Battery lifetime

The battery lifetime of the probe during continuous motion was evaluated by mounting the probe to a drill (sampling at an interval of 100 ms). After approximately 15 min of continuous drilling, the internal memory was filled. Once the memory was filled, the data were transferred via the gateway and the memory subsequently cleared. The procedure was repeated until the battery voltage dropped below the critical threshold for probe operation.

Five data acquisition and download cycles could be completed during two tests with activated accelerometer and magnetometer (i.e. without gyroscope). After the fifth cycle, the memory could be filled to approximately 50% before the battery was empty. When the gyroscope was additionally activated, only two to three complete cycles were possible. Repeating the tests with different power settings resulted in four cycles and 20% filled memory for the lowest power setting (highest noise – lowest power), four cycles and 25% filled memory for the default setting (noisy – low power) and almost four cycles (the battery died during data download) for the highest power setting (lowest noise – highest power). 1.5 additional cycles were possible when using high quality batteries from a different producer. To summarize: Three to four cycles are feasible with high quality batteries and all the three sensors activated, almost independent of the power setting.

Consequently, the battery lifetime and though the operation time of the probe depends mainly on the battery quality and on which sensors are turned on. The power settings have a minor influence. Other conditions such as temperature will also influence the battery lifetime but have not been tested specifically.

3.3. Sample application: Smartstone embedded in a pebble

3.3.1. Flume and camera setup

The performance of a Smartstone probe embedded in a pebble (Fig. 1c) was tested in a series of preliminary experiments, which were carried out in a 2.7 m long and 0.265 m wide flume at the Trier University, Germany. In these tests, the flume's slope was adjusted to an angle of 11° to enable large pebble velocities resulting from flow forces supported by gravity forces. The flume was formerly used to analyse pebble movement patterns in the context of soil erosion (Becker et al., 2015). In the corresponding experiments, the mouldable soil surface in natural rills was imitated by covering the flume bottom with floral foam. The same foam was used in the present experiments. The water was recirculated in the flume by an electrical effluent pump with a maximum discharge of 4.6 l s^{-1}. In the tests, the pump was run slightly below maximum capacity resulting in a flow velocity of ≈ 1 m s^{-1} at a water depth of ≈ 1.2 cm.

3.3.2. Probe installation

In the following, we present and discuss data obtained in a specific experiment with the tracer pebble shown in Fig. 1c, which was selected from a range of differently shaped tracer stones (Becker et al., 2015). The pebble, which was specified in Section 3.1, was painted with black and white patterns, which were aligned with the pebble's main axes (Fig. 1c) to facilitate image analysis.

In order to equip the pebble with the Smartstone probe, a hole with a diameter of 8 mm was drilled into the pebble. The hole is located at the point, where the lines of the pebble's painting intersect at the end of the pebble's long axis. The 60 mm deep hole was precisely aligned with the longest axis. Next to this hole, a second hole with a 3 mm diameter was drilled for the antenna. For optimal signal transmission, the angle between both holes should be approx. 30°. Afterwards, 2–3 mm of the partition wall between the two holes was removed to route the flexible antenna. The probe was inserted completely into the bigger hole and the antenna was routed to the other hole. The bend part at the holes' ends was covered with a piece of paper to prevent it from gluing to the waterproof modelling mass, with which the holes were sealed at the end. The modelling mass was moulded to recover the original shape of the pebble.

As mentioned above, special care was taken to align the probe coordinate system with the pebble axes, i.e. the pebble a-axis with the long

axis of the cylinder (green axis in Fig. 1b), the b-axis with the red cylinder axis in Fig. 1b (which was defined to be vertical when the battery screw was located on top of the probe), and the c-axis with the blue-sensor axis (which is orthogonal to the red cylinder axis in Fig. 1b).

The alignment of the Smartstone probe and the colour code with the pebble's main axes has two main advantages: Centring avoids additional centrifugal forces, which superimpose the accelerations captured by the accelerometer (gravity and relevant changes in velocity); and the comparison of Smartstone data with image data is much more straightforward.

Including the probe, the pebble weighed 0.2867 kg. For this specific pebble, the sensor installation changed the total weight only by 0.0005 kg. For different stone densities, the aforementioned centred installation is even more important to influence the kinetic behaviour of the stone as little as possible.

In order to gain independent data with regard to pebble movement, the pebble's motion was additionally recorded using an Optronis CR4000x2 high-speed camera (see also Becker et al., 2015). The camera was placed perpendicularly to the middle of the working range of the flume at a distance of 3 m and captured hence a large portion of the working section. The camera was inclined by 11° to align the flume's longitudinal axis with the camera frame. The frame rate of the camera was 250 frames per second and the image resolution 2304 × 1720 pixels (one pixel ≈ 0.8 mm of the flume).

At the beginning of an experimental run, the pebble was manually placed at the top of the flume in the flume centreline, with its a-axis perpendicular to the flow direction. The pebble was inserted into a small recess area in the floral foam to prevent its movement without external forcing. Before data acquisition, the Smartstone memory was cleared, the database emptied and the probe was directly set to recording mode with a sampling interval of 12 ms. The data acquisition by the Smartstone was initiated by switching on the pump, which caused the movement of the pebble. The high-speed camera measurements were manually started at approximately the same time. After the pebble reached the flume's end, the Smartstone data were transmitted, labelled and stored together with the high-speed images. The lateral movement of the pebble, which was not observable from the high-speed camera's point of view, was recorded by a conventional camera (25 fps), which was located at the flume's downstream end.

3.3.3. Merging high-speed images and Smartstone data

In order to facilitate the accurate comparison of the Smartstone data with the results from the image analysis, a synchronization of both data sets in time was required. The absolute point in time of each sample or image was not known, i.e. the start of the sampling of both data acquisition systems could not be triggered simultaneously. However, the aforementioned experimental procedure (initiation of pebble movement by switching on the pump and starting image acquisition manually at approximately the same time) allowed for the development of a software-based synchronization of both signals by shifting the Smartstone time series in time.

For this purpose, a new set of images was generated by a MATLAB script, containing the high-speed image information and Smartstone data (Fig. 2).

An instantaneous high-speed image, cropped to the section containing the relevant information, is shown in Fig. 2d. Fig. 2e presents the data acquired by the Smartstone probe (left: magnetometer; right: accelerometer; markers indicate the actual sample points in time). The black lines indicate the point in time corresponding to the shown high-speed image. The Smartstone data were shifted in time by adding an offset. The optimal offset was determined by shifting forward and backward in small increments until the magnetometer peaks coincide with the same pebble orientation within the whole image series. This offset is unique, as the rotation velocity changes over time. Therefore, only one specific offset will result in a match for the whole series. To facilitate the identification of the orientation, two aspects are useful: The axes orientation of the probe inside the pebble is known, as described in Section 3.3.2 and in Fig. 1b, and the direction and inclination of the earth's magnetic field relative to the flume has been determined. For the evaluation of the offset, also the accelerometer peaks (Fig. 2e, right chart) were used to check if the peaks coincide with the saltations of the pebble in the images. Note that in this specific case, the Smartstone data did not cover the experiment's beginning.

In Fig. 2a, bar charts visualize the Smartstone data tuple corresponding to the sensors reading at the point in time as indicated by the black lines in Fig. 2e. The scale was adjusted to the maximum values of each run (different measurement environments will result in different values of magnetometer due to the spatial variability of the earth's magnetic field).

The whole set of images was used to produce a video showing the complete run in slow motion (factor 40), see Video 1 in the online publication.

3.3.4. Deriving pebble orientation

The Smartstone probe measures data that can be used to reconstruct its orientation and movement as a function of time. As the Smartstone-kit presented in this Technical Note represents a prototype system, a methodology had to be developed to derive successive orientations from the sensor data. Therefore, a preliminary approach was developed by applying algorithms that are used for tilt-compensated compasses (e.g. Ozyagcilar, 2012). Such algorithms have been developed for devices that do not move during measurement. Applying these algorithms to the Smartstone pebble, the accelerometer readings could theoretically be used to estimate two angles of the orientation and the remaining angle using the magnetometer.

However, the Smartstone probe is moving so that the accelerometer does not only show gravity-induced accelerations but also motion related accelerations due to the forcing by water and the interaction of the pebble with the flume boundaries (walls and bed). To overcome this shortcoming, the more stable magnetometer values were used to estimate firstly the pitch (rotation around green axis in Fig. 1b, $\tan(\text{pitch}) = B_y/B_z$). This value was then used to rotate the sensor axes and estimate roll (rotation around the blue axis in Fig. 1b, $\tan(\text{roll}) = B_x/B_z$). If the sensor is rotated around the line of magnetic flux, the magnetometer readings will deliver constant values, as the angles do not change. Thus, the transformation from magnetometer readings to three angles – pitch, roll and yaw (rotation around red axis) – is not unique. The last value, yaw can only be derived by sensor fusion, i.e. the additional use of the accelerometer data. However, as pointed out before, these values are superimposed by accelerations caused by other parameters than gravity introducing deviations if they would not be filtered. Corresponding filters were not readily available and the obtained results for yaw were not satisfactory with this simple approach. Therefore, we decided to focus on pitch and roll, as the pebble did not change its rotation axis during the run. A rotated CAD-model of the pebble is shown in Fig. 2b showing the derived orientation of the pebble corresponding to the time indicated by the black lines in Fig. 2e. The supplementary online video shows the whole sequence.

3.3.5. Comparison of derived positions

Knowing the orientation of the pebble for each point in time, the corresponding accelerometer tuple can be rotated to be aligned with the flume's axes. One axis represents longitudinal acceleration (in flow direction), the next axis lateral acceleration and the third axis vertical acceleration. The pebble's velocity along each axis and its position can then be estimated based on kinematic principles. As the beginning of the run was not contained in the Smartstone data, the initial velocity for the first available data tuple was taken from image analysis. For the analysis of the high-speed images, the positions were derived by marking the left and right pebble boundary in each image, calculating the mean, and correcting the deviation resulting from the projection.

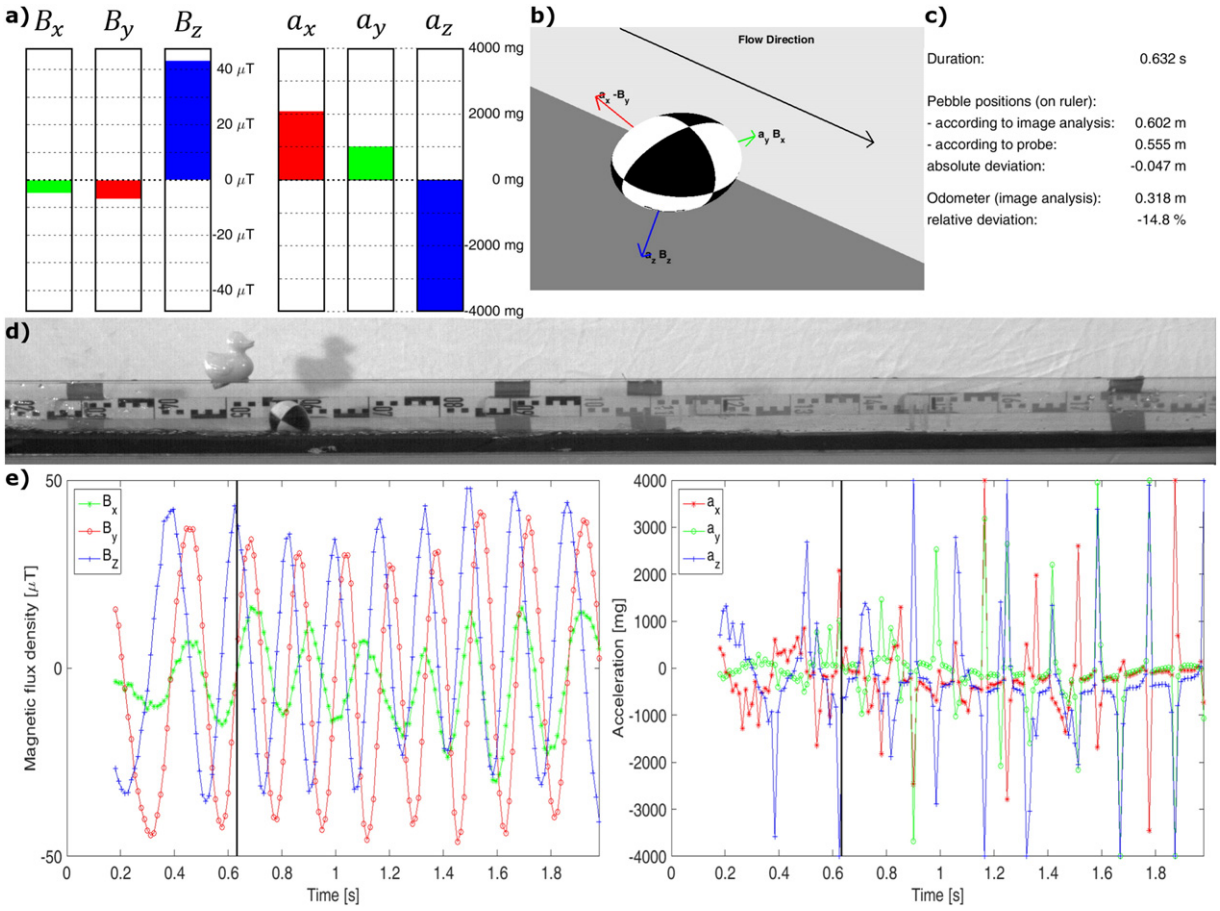

Fig. 2. Composition of (a) bar chart showing the sensor readings of the current point in time, (b) computer model illustrating the probe-derived pebble orientation of the current point in time, (c) summary of relevant data for the current point in time, (d) cropped high speed image of the current point in time and (e) Smartstone data charts showing the complete time series of magnetometer (left) and accelerometer (right); the black vertical lines indicate the current point in time of the complete frame.

Fig. 2c presents the derived longitudinal position of the pebble from both the Smartstone data and image analysis at the indicated point in time (i.e. black lines in Fig. 2e); the reference for the derived values is the ruler shown in Fig. 2d. We focused solely on the determination of the longitudinal movement, as the transverse and vertical movement were negligible compared to the longitudinal movement due to the narrow flume width and transport as bed load. Moreover, the corresponding values are rather uncertain due to several reasons that will be discussed later. Besides the positions as seen on the ruler, the odometer shows the total distance from the starting position to the current position. The last value in Fig. 2c shows the relative deviation of the probe-derived position, which is the percentage of absolute deviation as a fraction of the odometer.

3.3.6. Results and discussion

In the following, several interesting issues contained in the dataset will be highlighted and discussed. They are visible in Video 1 and their identification can be facilitated by using the repeat and pause functions of the video player.

Firstly, the magnetometer readings B_y and B_z (red and blue lines in Fig. 2e, left chart) show a sinusoidal development. For example the readings B_z (blue line) show their first minimum at 0.220 s. The second minimum is at 0.516 s; the first rotation takes 0.296 s. The third minimum is at 0.728 s; the second rotation takes 0.212 s. The forth minimum is at 0.904 s; the third rotation takes 0.176 s. This decrease in period is caused by the acceleration of the pebble. Thus, analysing the periods in more detail allows for the determination of the rotation speed and the number of rotations. The offset between the B_y and B_z time series is π/2, as these two axes are perpendicular to each other.

For the accelerometer time series (Fig. 2e, right chart), only the first rotation is visible: values change from $a_Z \approx 1000$ mg to $a_Z \approx -1000$ mg within half a rotation. Afterwards, the acceleration values are influenced by additional forces apart from gravity. Finally, when the pebble reaches its terminal velocity after approx. 1.5 s, it touches ground only twice during each rotation and saltates in between: all accelerometer values are close to zero, interrupted by peaks with alternating signs.

For the whole duration, the readings of the Smartstone can be comprehended by image analysis: peaks of magnetometer readings occur always for the same rotation angle; impacts shown in accelerometer data coincide with bounces visible in image data.

However, there are several deviations visible in the orientation visualization, e.g. after 0.532 s, 0.716 s or 0.936 s etc. in Video 1. One of the main reasons might be the unstable magnetic field in the laboratory. It was found that the resultants of the magnetometer values fluctuated between 26 and 51 μT during the run. Additional tests with a conventional compass, which was positioned at several places in the flume, confirmed this result as the indicated direction to magnetic north deviated up to 20° for single positions. This may be caused by the metal frame of the flume or additional sources (such as light, electric equipment), which can influence the magnetic field.

A second aspect worth discussing is the deviation of the derived positions (Video 1). The position derived from image analysis is biased up to +/−0.03 m, as the correction of the projection is only valid as long as the pebble remains in the centre of the flume (which it did not). Nevertheless, these deviations and the respective correction are limited as

mentioned above to approx. 0.03 m at the left and right end of the image. This indicates that the observed deviation is mainly due to the Smartstone data. There are mainly five different reasons for these deviations, ordered by magnitude:

1. The quantisation error is an intrinsic reason: the precision of the values is limited. For the chosen range of 4 g, the resolution is 2 mg. Assuming that the true values are rounded during quantization, the upper boundary for the difference between the true value and the displayed value is 1 mg. For the duration of our experiment (≈2 s), the maximum deviation resulting from quantisation error is 0.0196 m ($s = 0.5\ a\ t^2$, where s denotes the distance, a the acceleration in m s^{-2} and t the time). If the range of the accelerometer is increased to the maximum of +/− 16 g, the maximum error after 2 s increases to 0.0785 m. The fraction of deviation resulting from this source will differ with the duration of the experiment and the magnitude of acceleration.
2. Noise: The noise depends on the setting: For the lowest power consumption and 12 ms sampling intervals, the noise is 10 mg. For highest power consumption and intervals greater than 24 ms, the noise drops to 1.2 mg. The given values are root mean square errors. Without further assumptions concerning their distribution, the resulting deviation cannot be estimated, but will later be evaluated empirically.
3. Integration error: the estimation of the position from kinematic principles is based on double integration, thus errors are integrated twice. It is a numerical integration of values with finite time steps and data that is sampled with a finite sampling rate. This error is intrinsic to the method and consequently, the derived position will always increasingly differ over distance *and* time (the derived position of a pebble not moving will tend to move).
4. Orientation error: the derived orientation was used to align the accelerometer readings to the flume. These orientations are imprecise, and thus, the derived velocity and position are defective, too. If the orientation is off by only 1°, the gravity residuals for the axis perpendicular to the gravity vector will be 17.45 mg (sin(1°) 1000 mg). This results in a deviation of 0.3424 m after 2 s.
5. Clipping error: this important reason becomes apparent from Fig. 2e (and/or the online video): Several values of the accelerometer were outside the measurement range of +/− 4000 mg. There is even more evidence for this conclusion: The pebble bounces several times in an angle stressing two axes a_y and a_z (e.g. at 1.164 s) and sometimes even all three axes (e.g. at 1.872 s). In the latter case, all axes show the maximum value (resultant 6.928 g). If an impact of the same magnitude occurs in a different orientation of the pebble stressing only one axis (force aligned with one axis), this impact would have been clipped. The effect is also visible in the video: The deviation increases monotonically until the first big impact occurs after 0.624 s. Then the deviation remains almost stable until the next big impact after 1.164 s. After this point in time, the deviation starts to increase faster. The influence of this clipping is very strong: If the pebble is accelerated with 4000 mg for 12 ms, the resulting velocity is 0.47 m s^{-1}. If the true acceleration was 6928 mg, the resulting velocity is 0.8146 m s^{-1}. The deviation in the position estimation due to this difference between true velocity and estimated velocity will increase with time: it will increase by 0.3446 m every second for only one clipped peak.

To support this theoretical argumentation, additional experiments were conducted to disentangle the different reasons for deviations. Their results are shown in Table 1.

The second column shows the results of the first experiment in which the sensor was mounted to a cart thereby being precisely aligned with the cart trajectory to stress only one axis. The cart was then moved 5 times for 1.5 m, which corresponds to the same travel distance as in the laboratory flume. The duration of each move was approx. 2 s. Afterwards, the distance was derived from the sensor data resulting in a mean absolute deviation of 3.32% and a standard deviation of 4.03%. These deviations are due to quantisation error, noise, integration error and the true deviation of the travelled distance to 1.5 m.

The third column of Table 1 shows the results of the second experiment. In this test, the sensor setting was changed to lowest power consumption and 12 ms sampling intervals, which resulted in increased noise. The deviations were smaller compared to the 24 ms intervals, which does not perfectly agree with theory.

In a further experiment, the sensor was mounted in a cylinder rolling down a ramp outside of a building, avoiding acceleration peaks above 4000 mg. The distance was again 1.5 m, the inclination was the same as in the laboratory flume, the movement's duration was approx. 2 s. In this type of experiment, the orientation error is added, but the error is smaller compared to the laboratory flume where the earth's magnetic field is disturbed by the flume's metal frame. Analysing the measurements, the mean absolute deviation increased to 13.74%.

Following the rolling-test, the same cylinder was moved without water in the laboratory flume, introducing the deviations resulting from the disturbed magnetic field. Consequently, the mean absolute deviation increased to 21.65%.

Finally, several runs of the actual laboratory flume experiment were evaluated (first run is the run shown in the video), which includes strong clipping. Considering these experiments, the mean absolute deviation increased to 63.18%. In the runs showing the largest deviation, the pebble hit the flume's sidewalls, which resulted in maximum accelerometer readings.

We conclude that the orientation and clipping errors are the main reasons for the observed deviations. However, both of them can be reduced in future applications as the presented preliminary analysis is based on a simple approach to derive the orientation in order to test the general applicability of the Smartstone. In fact, there exist many more sophisticated methods such as Kalman filtering or hidden Markov models, which are well established in other disciplines like computer science, robotics or (pedestrian) navigation. Both methods can be used to calculate probabilities of certain orientations taking into account respective uncertainties and the temporal development of the movement. As we also generate three-dimensional models of the experimental environment (Brings et al., 2015), it might even be possible to apply a probabilistic map based localization like Markov localization (e.g. DeSouza and Kak, 2002; Fox et al., 1998).

Table 1
Summary of five runs of five different experimental settings, which incorporate increasing numbers of deviation reasons from left to right.

	One axis, 24 ms sampling (low noise)	One axis, 12 ms sampling (high noise)	Smooth rolling, undistorted magnetic field	Smooth rolling, laboratory flume	Pebble with acceleration peaks in laboratory flume
1st run	−3.0%	−5.3%	7.9%	−28.1%	32.4%
2nd run	−4.3%	−4.0%	−1.9%	−15.1%	30.7%
3rd run	1.9%	−0.9%	32.3%	10.8%	−58.5%
4th run	5.3%	4.5%	−1.8%	35.0%	131.3%
5th run	−2.6%	−1.0%	−21.8%	24.8%	−75.2%
Mean absolute deviation	3.3%	2.6%	13.7%	21.7%	63.2%
Standard deviation	4.0%	3.8%	19.7%	26.6%	83.0%

The clipping issue with regard to the accelerometer might be easier to tackle as it has an adjustable range up to +/− 16 g (Bosch Sensortec, 2014) and the extended range will therefore be implemented in the probe's next generation. However, changing the measuring range, the discretization gets coarser (8 mg) and thus, the quantisation and integration errors may become more significant. The user has to consider the suitable range according to the expected magnitude of impacts, which will vary strongly for different applications, e.g. a soft mouldable wet soil surface, as imitated by the floral foam in the here described experiments, or stony surfaces without any dampening characteristics.

4. Summary and outlook

The described Smartstone probe fits into stones with a longest axis exceeding 60 mm and allows for tracking of their movement in water using wireless signal transfer, identification by an active RFID tag and a 9-axis sensor module. The qualitative results from a first application with a pebble rolling down a flume clearly show a rotation of the pebble indicated by both the accelerometer and the magnetometer values. A sampling interval of 12 ms was sufficient to track the movements avoiding sub-Nyquist sampling. The gyroscope data were omitted because the gyroscope is linked to a maximum sampling frequency of 10 Hz. Increased measuring frequency reduces the possible measuring time due to limited memory and increases the duration of data transmission. The pictures of the high-speed camera are suitable as reference of the real movement. In addition, they support the understanding of Smartstone data and their interpretation in a sense of three-dimensional movement. Even with simple approaches, it is possible to estimate a rough orientation and derive probe positions. These quantitative results can still be optimized by more sophisticated post-processing of the acquired data.

For the next probe generation, an additional mode will be introduced, which adjusts the accelerometer's range to +/− 16 g.

In the geomorphological context, the probe will by applied in rill erosion experiments like described in Wirtz et al. (2012). The sample application showed the principal applicability of the probe for these experiments, where a high-speed camera cannot be used for several reasons like turbid water etc. Here, one long-term objective is to derive complete movement patterns like published in Becker et al. (2015) directly from Smartstone data.

Furthermore, the Smartstone probe will be used in physical model testing of riprap in hydraulic engineering. Experiments will include small-scale laboratory model testing as well as large-scale tests in the field (Hiller and Lia, 2015).

The applicability of the probe in different conditions – e. g. increased water depth or the probe being buried in sediment – is still to be tested as these obstacles will dampen the signals used for data transfer. However, the magnitude of this effect is difficult to predict.

Besides these applications, it has to be checked if the accuracy of the Bosch 9-axis sensor is preserved in the composite of the Smartstone probe.

Supplementary data to this article can be found online at http://dx.doi.org/10.1016/j.catena.2016.03.030.

Acknowledgements

We thank SST (smart sensor technologies) Rheinberg (contact: info@smart-sensor-technologies.de) for the collaboration with the development of the Smartstone measuring equipment. We also thank Bosch Sensortec for letting us use their pictograms in the Graphical Abstract. Furthermore, we appreciate the help of the students Jens Jakobsen and Johannes Kobel for the evaluation of battery lifetime and range. The financial support from Energy Norway and the Research Council of Norway within the project 235730 is acknowledged.

References

Becker, K., Gronz, O., Wirtz, S., Seeger, M., Brings, C., Iserloh, T., Casper, M.C., Ries, J.B., 2015. Characterization of complex pebble movement patterns in channel flow — a laboratory study. Cuadernos de Investigación Geográfica 41 (1).

Bedeus, K., Ivicsics, L., 1963. Observation of the noise of bed load. In: Land Erosion Precipitations, Hydrometry, Soil, Moisture (Proc. Berkeley Assembly, August 1963). Publ. Int. Assoc. Sci. Hydrol. 384–390.

Brings, C., Gronz, O., Becker, K., Wirtz, S., Seeger, M., Ries, J.B., 2015. 3D surface reconstruction and volume calculation of rills. Geophysical Research Abstracts. Presented at the EGU General Assembly, European Geosciences Union.

Cameron, C., 2012. A wireless sensor node for monitoring the effects of fluid flow on riverbed sediment. Univ. Glasg. Sch. Comput. Sci. Level 4 Project, p. 70.

De Jong, C., 1991. A re-appraisal of the significance of obstacle clasts in cluster bedform dispersal. Earth Surf. Process. Landf. 16 (8), 737–744.

DeSouza, G.N., Kak, A.C., 2002. Vision for mobile robot navigation: a survey. IEEE Trans. Pattern Anal. Mach. Intell. 24, 237–267.

Ergenzinger, P., De Jong, C., 2003. Perspectives on bed load measurement. IAHS Publ. 113–125.

Ergenzinger, P., Schmidt, K.-H., Busskamp, R., 1989. The pebble transmitter system (PETS): a technique for studying coarse material erosion, transport and deposition. Z. Für Geomorphol. 33, 503–508.

Ergenzinger, P., de Jong, C., Laronne, J., Reid, I., 1994. Short term temporal variations in bed load transport rates: Squaw Creek, Montana, USA and Nahal Yatir and Nathal Eshtemoa, Israel, in: Dynamics and Geomorphology of Mountain Rivers (ed. by P. Ergenzinger & K.-H. Schmidt). Springer, Berlin, pp. 251–264.

Foster, D.I., 2000. Tracers in Geomorphology. John Wiley & Sons, Chichester, UK.

Fox, D., Burgard, W., Thrun, S., 1998. Active Markov localization for mobile robots. Robot. Auton. Syst. 25, 195–207. doi:http://dx.doi.org/http://dx.doi.org/10.1016/S0921-8890(98)00049-9

Gray, J.R., Gartner, J.W., Barton, J.S., Gaskin, J., Pittman, S.A., Rennie, C.D., 2010. Surrogate technologies for monitoring bed-load transport in rivers. Sedimentol. Aqueous Syst. 46–79.

Habersack, H., 1997. Raum-Zeitliche Variabilitäten im Geschiebehaushalt am Beispiel der Drau. Universität für Bodenkultur, Wien.

Hiller, P.H., Lia, L., 2015. Practical challenges and experience from large-scale overtopping tests with placed riprap. In: Toledo, M.Á., Morán, R., Oñate, E. (Eds.), Dam Protections against Overtopping and Accidental Leakage. CRC Press/Balkema, London, pp. 151–157.

Johnson, P., Muir, T.C., 1969. Acoustic detection of sediment movement. J. Hydraul. Res. 7, 519–540.

Krause, L., 1997. Neue Wege zur Entwicklung von zeitlich hochaufgelösten Meßtechniken des Grobgeschiebetransportes. Institut f. Geographische Wissenschaften, Freie Universität Berlin, Berlin (Diploma Thesis).

Krein, A., Klinck, H., Eiden, M., Symader, W., Bierl, R., Hoffmann, L., Pfister, L., 2008. Investigating the transport dynamics and the properties of bedload material with a hydroacoustic measuring system. Earth Surf. Process. Landf. 33, 152–163. http://dx.doi.org/10.1002/esp.1576.

Lamarre, H., Roy, A.G., 2008. The role of morphology on the displacement of particles in a step–pool river system. Geomorphology 99, 270–279. http://dx.doi.org/10.1016/j.geomorph.2007.11.005.

Liébault, F., Bellot, H., Chapuis, M., Klotz, S., Deschâtres, M., 2012. Bedload tracing in a high-sediment-load mountain stream. Earth Surf. Process. Landforms 37, 385–399. http://dx.doi.org/10.1002/esp.2245.

Oikawa, Y., 2011. Tag movement direction estimation methods in an RFID gate system, in: In: C. Turcu (Ed.): Current Trends and Challenges in RFID. pp. 441–455.

Ozyagcilar, T., 2012. Implementing a Tilt-Compensated eCompass Using Accelerometer and Magnetometer Sensors (Application Note No. AN4248), Freescale Semiconductor.

Reid, I., Layman, J., Frostick, L.E., 1980. The continuous measurement of bed load discharge. J. Hydraul. Res. 18, 243–249.

Ryan, S.E., Bunte, K., Potyondy, J.P., 2005. Breakout session II, Bedload-transport measurement: data needs, uncertainty, and new technologies. Proceedings of the Federal Interagency Sediment Monitoring Instrument and Analysis Workshop. Circular.

Schaffernak, F., 1916. Die Theorie des Geschiebetriebes und ihre Anwendung. Z. Oesterreichischen Ing.- Archit.-Ver. 11.

Schneider, J.M., Hegglin, R., Meier, S., Turowski, J.M., Nitsche, M., Rickenmann, D., 2010. Sudying Sediment Transport in Mountain Rivers by Mobile and Stationary RFID Antennas. In: Dittrich, A., Koll, K., Aberle, J., Geisenhainer, P. (Eds.), Proceedings of the International Conference on Fluvial Hydraulics: River Flow 2010. Bundesanstalt für Wasserbau, Braunschweig, pp. 1723–1730.

Sensortec, Bosch, 2014. BMX055 Small, Versatile 9-Axis Sensor Module, Data Sheet.

Wirtz, S., Seeger, M., Ries, J.B., 2012. Field experiments for understanding and quantification of rill erosion processes. Catena 91, 21–34.